Journal of Alloys and Compounds 509 (2011) 4896–4904

Contents lists available at ScienceDirect

Journal of Alloys and Compounds

journal homepage: www.elsevier.com/locate/jallcom

Gas atomization of Cu-modified AB_5 metal hydride alloys

K. Young[a,*], T. Ouchi[a], A. Banik[b], J. Koch[a], M.A. Fetcenko[a], L.A. Bendersky[c], K. Wang[c], M. Vaudin[d]

[a] Energy Conversion Devices Inc./Ovonic Battery Company, 2983 Waterview Drive, Rochester Hills, MI 48309, USA
[b] Special Metal Corporation, 100 Industry Lane, Princeton, KY 42445, USA
[c] Materials Science & Engineering Laboratory, National Institute of Standards and Technology, Gaithersburg, MD 20899, USA
[d] Ceramics Division, National Institute of Standards and Technology, Gaithersburg, MD 20899, USA

ARTICLE INFO

Article history:
Received 29 December 2010
Received in revised form 19 January 2011
Accepted 28 January 2011
Available online 22 February 2011

Keywords:
Hydrogen absorbing materials
Transition metal alloys
Metal hydride electrode
Electrochemical reactions

ABSTRACT

Gas atomization together with a hydrogen annealing process has been proposed as a method to achieve improved low-temperature performance of AB_5 alloy electrodes in Ni/MH batteries and restore the original cycle life which was sacrificed by the incorporation of copper in the alloy formula. While the gas atomization process reduces the lattice constant aspect ratio c/a of the Cu-containing alloys, the addition of a hydrogen annealing step recovers this property, although it is still inferior to the conventionally prepared annealed Cu-free alloy. This observation correlates very well with the cycle life performance. In addition to extending the cycle life of the Cu-containing metal hydride electrode, processing by gas atomization with additional hydrogen annealing improves high-rate, low-temperature, and charge retention performances for both Cu-free and Cu-containing AB_5 alloys. The degradation mechanisms of alloys made by different processes through cycling are also discussed.

© 2011 Elsevier B.V. All rights reserved.

1. Introduction

The nickel/metal hydride (Ni/MH) battery was invented to replace the nickel cadmium (NiCd) battery because of environmental concerns related to the toxicity of cadmium. Except for low-temperature performance, almost all Ni/MN battery performance characteristics are comparable to NiCd battery with the only exception in low temperature. The operational temperature of NiCd battery can be extended to −40 °C while commercially available Ni/MH battery can only go as low as −20 °C [1,2]. The capability of operating a hybrid electrical vehicle in severe winter condition necessitates improved low-temperature performance of Ni/MH battery [3].

Copper had been previously employed as a substitutional element in the metal hydride (MH) alloys to partially replace the more expensive cobalt and therefore lower the alloy cost [4–14]. However, the replacement resulted in severe cycle life performance degradation in these Co-free or low-Co alloys. Copper was found to be the most effective substitutional element in improving the low-temperature power performance of AB_5 Ni/MH battery due to its ability to modify the surface oxide by filling it with voids, tunnels, and metallic scrolls instead of regular granular shapes [4]. However, the incorporation of Cu in the AB_5 alloy degrades certain performance characteristics due to the decrease in the lattice constant ratio c/a increasing both the hydrogen absorption/desorption hysteresis and the pulverization rate of the particles [5].

Several methods in composition design, such as adding Zr and/or Si and hyper-stoichiometry, had been proposed to compensate for the negative effect that incorporation of Cu has on cycle life [15–17]. Fast quench from the melt using gas atomization (GA) was demonstrated for the Cu-containing AB_5 alloys as a mean to extend cycle life [18], but the high-rate charge/discharge characteristics of the alloy were hindered. In this paper, we propose to combine GA and annealing in hydrogen (AH) processes to further extend the cycle life of the Cu-containing AB_5 alloys. Similar work has been performed on the Laves phase based AB_2 alloys and the results were very encouraging [19,20]. While GA alone provides advantages of lowering production cost and extending cycle life, the additional hydrogen annealing further improves the capacity, formation, high-power, and low-temperature performance of these MH alloys.

2. Experimental

Details of the conventional melt-and-cast and GA processes can be found in another publication [20]. Some of the conventional melt-and-cast ingot was set aside for later use as pre-alloyed charge material for GA processing. The balance of the ingot was annealed in a vacuum furnace at 950 °C for 8 h before being mechanically pulverized to 200 mesh powder. The AH process used a commercial hydrogen annealing furnace retrofitted by Heat Source Inc., Dallas, TX.[1] The gas flow was set

* Corresponding author. Tel.: +1 248 293 7000; fax: +1 248 299 4520.
E-mail address: kwoyoung@yahoo.com (K. Young).

[1] Manufacturer names are included for completeness. Their mention does not constitute an endorsement by NIST.

0925-8388/$ – see front matter © 2011 Elsevier B.V. All rights reserved.
doi:10.1016/j.jallcom.2011.01.204

Table 1
Compositions of design, mother ingot, annealed ingot, gas atomized powder before and after annealing in hydrogen in atomic percentage determined by ICP. Only 5–10% of La was lost in the GA process due to the oxidation and slug formation.

	La	Ce	Pr	Nd	Ni	Co	Mn	Al	Cu	Fe
C1 target	10.5	4.3	0.5	1.4	64.3	8.4	4.6	6.0	0.0	0.0
C1 mother ingot	10.2	4.8	0.5	1.4	64.3	8.5	4.7	5.4	0.0	0.2
C1 after annealing	10.0	4.8	0.5	1.3	64.5	8.5	4.7	5.5	0.0	0.2
C1 gas atomized	9.5	4.4	0.5	1.4	65.3	8.4	4.6	5.8	0.0	0.1
C1 GA with AH	9.5	4.3	0.5	1.4	65.2	8.5	4.6	5.9	0.0	0.1
C2 target	10.5	4.3	0.5	1.4	64.3	5.0	4.6	6.0	3.4	0.0
C2 mother ingot	10.7	4.5	0.4	1.3	63.8	5.1	4.7	5.9	3.5	0.1
C2 after annealing	10.8	4.2	0.4	1.3	64.4	5.2	4.6	5.6	3.4	0.1
C2 gas atomized	9.4	4.5	0.4	1.2	65.6	5.1	4.5	5.8	3.4	0.1
C2 GA with AH	9.4	4.5	0.4	1.3	65.3	5.1	4.6	5.8	3.5	0.1
C3 target	10.5	4.3	0.5	1.4	64.3	3.0	5.9	4.7	5.4	0.0
C3 mother ingot	10.5	4.6	0.5	1.4	64.5	2.8	5.6	4.5	5.5	0.1
C3 after annealing	10.9	4.2	0.4	1.3	64.4	3.2	5.7	4.6	5.3	0.0
C3 gas atomized	9.9	4.3	0.5	1.3	65.0	2.9	5.8	4.7	5.5	0.1
C3 GA with AH	10.0	4.3	0.5	1.4	64.8	3.1	5.8	4.6	5.4	0.1

to be 20 l/min, the load size was up to 20 kg, and the time duration at 950 °C was 30 min. This annealing condition was optimized by tracking the reduction of the saturated magnetization (M_S) of AB_2 alloys [20]. After the AH process, the sample was then allowed to cool down to room temperature in a flowing argon environment. The chemical composition of each sample was examined by a Varian *Liberty 100* inductively coupled plasma (ICP) system. A Philips *X'Pert Pro* X-ray Diffractometer (XRD) was used to study the microstructure of each alloy, and a JOEL-*JSM6320F* SEM with X-ray energy-dispersive spectroscopy (EDS) capability was used to study the phase distribution and the composition. Phase analysis was carried out using electron back scatter diffraction (EBSD) in a Hitachi 4700 scanning electron microscope (SEM). Pressure–concentration–temperature (PCT) characteristics were measured using a Suzuki-Shokan multi-channel PCT system. In the PCT analysis, each sample was first activated by a 2 h thermal cycle between 300 °C and room temperature at 2.5 MPa H_2 pressure. The magnetic susceptibility (MS) measurement was performed on a Princeton Measurements Corporation *MicroMag 2900* alternating gradient magnetometer. Details of both electrode and cell preparations as well as measurement methods had been reported previously [21].

3. Results and discussion

3.1. Chemical composition

For the primary ingots, three La-rich misch-metal[2] based AB_5 alloy compositions were selected with Cu contents of: 0.0 at.% (C1), 3.4 at.% (C2), and 5.4 at.% (C3) at the expense of Co, respectively. The Mn/Al contents were slightly modified in C3 to further increase the surface reactivity [22,23]. The designed chemical compositions of these three alloys are listed in Table 1 together with the compositions of the alloys at different stages of processing. Comparing the composition of the primary ingots produced by the induction melting to the target value, the followings are found: a small deviation in La is caused by the inhomogeneity of the misch-metal raw material, a small amount of Al is lost as a contribution to the slag formation, and a small amount of Fe pick-up is from the wall of a cooling mold.

The composition does not change with the annealing process. The composition of the GA powder has a lower La content compared to the primary ingot due to a preferential oxidation by the presence of gas impurities and refractory interactions during the second melt resulting in the formation of La_2O_3 slag, which is later removed by the use of a tundish. There is no Fe-pickup because the powder solidifies in flight prior to contact with the collection chamber.

[2] Misch-metal is an alloy of rare earth elements in various naturally occurring proportions.

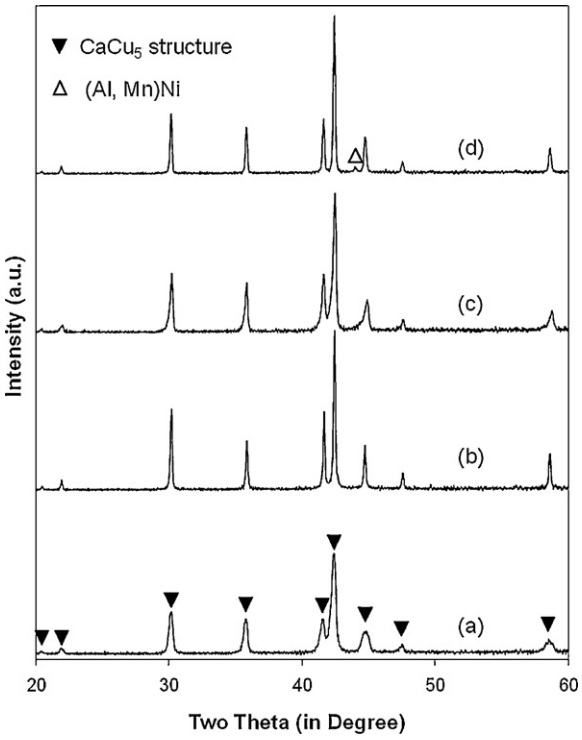

Fig. 1. XRD spectra using Cu Kα as the radiation source for alloys with C1 composition and prepared by melt-and-cast (a), melt-and-cast with annealing in 950 °C vacuum (b), gas atomization (c), and gas atomization with annealing in 950 °C hydrogen (d).

3.2. Microstructure study using XRD analysis

The microstructures of C1, C2, and C3 alloys prepared by melt-and-cast with (MCA) and without (MC) vacuum annealing at 950 °C, and gas atomization powder with (GAAH) and without (GA) annealing in hydrogen were studied by XRD analysis. The resulting spectra are plotted in Figs. 1 (C1), 2 (C2), and 3 (C3) and the important parameters obtained from this analysis are listed in Table 2.

The as-prepared alloys show a typical $CaCu_5$ structure with broader peaks indicating a smaller grain structure [24] (Figs. 1a, 2a, and 3a). After vacuum annealing, the basic structure remains unchanged but the grain size increases as can be seen from the narrowing of the diffraction peaks (Figs. 1b, 2b, and 3b). The gas atomized alloys still show only the $CaCu_5$ structure with slightly narrower (Fig. 1c), same (Fig. 2c), and broader (Fig. 3c) peak widths comparing to those from the primary ingots. However, after annealing in hydrogen, the gas-atomized alloys exhibit small BCC peaks related to AlNi, MnNi, or (Al, Mn)Ni (Figs. 1d, 2d, and 3d). The positions of the (Al, Mn)Ni peaks for samples C1 and C3 are between the individual peaks from AlNi and MnNi shown by sample C2. The peak widths of all annealed samples, regardless of vacuum or hydrogen annealing, are very similar, as the annealing temperature is identical for each process (950 °C).

The lattice constant aspect ratio c/a is an important parameter that can be correlated to the degree of pulverization during cycling [5]. The c/a values of the three as-cast samples are almost identical. The annealing in the as-cast copper free ingot increases the c/a value from 0.8062 to 0.8093, which indicates an improvement in cycle life. However, the same annealing does not improve the c/a values of the copper containing alloy samples. This is the reason that the substitution of Cu for Co deteriorates the cycle life of the annealed sample. The experimental results indicate that the GA process reduces the c/a ratio, which is opposite to what has been previously reported on $Mm(Ni, Co, Mn, Ti)_5$ [25,26] and Mm(Ni, Co,

Table 2
Summary of XRD results for alloys with compositions C1, C2, and C3 by three different preparation methods.

Composition #	Preparation	Lattice cont. *a* in $CaCu_5$ (Å)	Lattice cont. *c* in $CaCu_5$ (Å)	*c*/*a* ratio	$CaCu_5$ unit cell volume (Å^3)	FWHM of $CaCu_5$ (0 0 1)	Phase summary
C1	MC	5.0135	4.0418	0.8062	87.978	0.335	$CaCu_5$
C1	MCA	5.0030	4.0488	0.8093	87.762	0.156	$CaCu_5$
C1	GA	5.0055	4.0292	0.8050	87.424	0.292	$CaCu_5$
C1	GAAH	5.0072	4.0469	0.8082	87.868	0.177	$CaCu_5$ + (Al, Mn)Ni
C2	MC	5.0145	4.0439	0.8064	88.059	0.262	$CaCu_5$
C2	MCA	5.0203	4.0498	0.8067	88.392	0.157	$CaCu_5$
C2	GA	4.9992	4.0274	0.8056	87.165	0.261	$CaCu_5$
C2	GAAH	4.9962	4.0373	0.8081	87.275	0.166	$CaCu_5$ + AlNi + MnNi + La_2O_3
C3	MC	5.0230	4.0507	0.8064	88.506	0.219	$CaCu_5$
C3	MCA	5.0215	4.0504	0.8066	88.447	0.163	$CaCu_5$
C3	GA	5.0040	4.0287	0.8051	87.361	0.307	$CaCu_5$
C3	GAAH	5.0165	4.0511	0.8076	88.286	0.156	$CaCu_5$ + (Al, Mn)Ni

Mn, Al)$_5$ [27] alloys. These reports indicated that a smaller *c*/*a* ratio creates more stress during the hydride-dehydride cycling. However, the spherical shape of a GA powder particle should be able to sustain a higher stress level without disintegration. After the AH process, it is noted that the *c*/*a* values of the three GA powder samples have increased. In the cases of copper-containing C2 and C3, the GAAH alloys show the largest *c*/*a* ratio in their series, and therefore improved cycle life performance is expected.

Comparing the unit cell volume among the different processing techniques, the GA samples are always the smallest with or without the copper substitution. The reduction in cell volume by the GA process agrees with previous reports on Mm(Ni, Co, Mn, Ti)$_5$ [25,26] and Mm(Ni, Co, Mn, Al)$_5$ [27] alloys. In most cases, the annealing process increases the unit cell volume.

3.3. Microstructure study using SEM/EDS

SEM secondary electron image (SEI) and backscattered electron image (BEI) micrographs of cross-sections of GA-C1, GA-C2, and

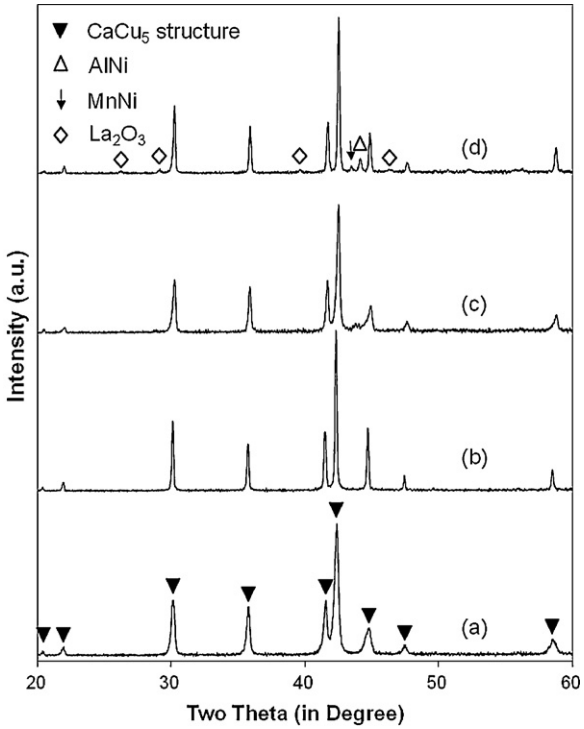

Fig. 2. XRD spectra using Cu Kα as the radiation source for alloys with C2 composition and prepared by melt-and-cast (a), melt-and-cast with annealing in 950 °C vacuum (b), gas atomization (c), and gas atomization with annealing in 950 °C hydrogen (d).

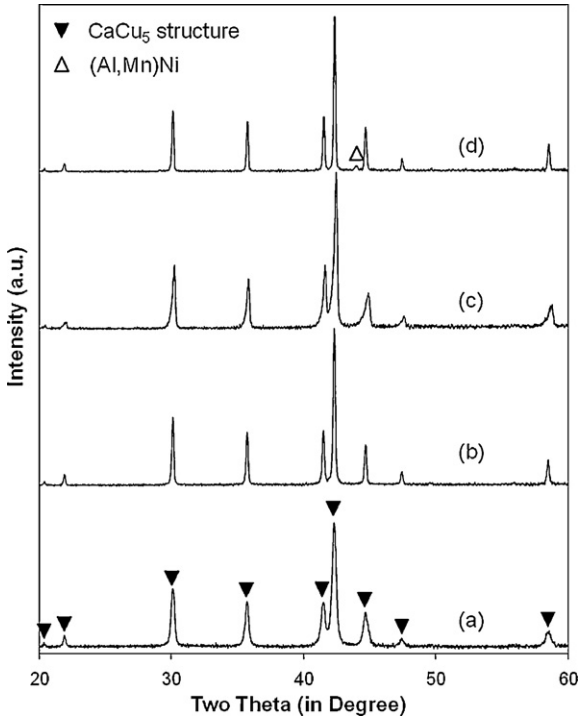

Fig. 3. XRD spectra using Cu Kα as the radiation source for alloys with C3 composition and prepared by melt-and-cast (a), melt-and-cast with annealing in 950 °C vacuum (b), gas atomization (c), and gas atomization with annealing in 950 °C hydrogen (d).

GA-C3 are shown in Fig. 4(a)–(f). In all three samples, a granular structure was observed, with the boundaries outlined in the BEI. The chemical compositions near the center (region 1) of the grain and across the boundary (region 2) were measured by EDS and the results are listed in Table 3. The grain boundary is rich in Mn and Al, and poor in Ni. However, the B/A stoichiometric ratio is higher in

Table 3
Composition in the area identified in SEM micrographs Fig. 4b, d, f, and h by EDS analysis. All numbers are in atomic percentages.

	La	Ce	Pr	Nd	Ni	Co	Mn	Al	Cu	B/A ratio
Fig. 4b-1	9.3	4.0	0.3	1.0	70.2	8.4	1.8	5.1	0.0	5.8
Fig. 4b-2	8.7	4.2	0.3	0.2	58.1	8.1	11.5	8.9	0.0	6.5
Fig. 4d-1	9.1	4.5	0.3	0.8	65.6	5.0	3.5	7.5	3.9	5.8
Fig. 4d-2	8.0	4.2	0.3	0.4	62.4	5.2	6.3	9.6	3.7	6.8
Fig. 4f-1	9.5	4.0	0.3	1.0	69.8	3.5	2.1	4.7	5.2	5.8
Fig. 4f-2	9.0	4.4	0.3	0.4	59.2	3.1	9.4	8.3	6.2	6.1
Fig. 4h-1	10.6	5.1	0.0	0.9	64.2	3.8	4.3	6.4	4.7	5.0
Fig. 4h-2	6.3	2.2	0.0	0.7	56.4	3.5	13.0	15.6	2.5	9.9

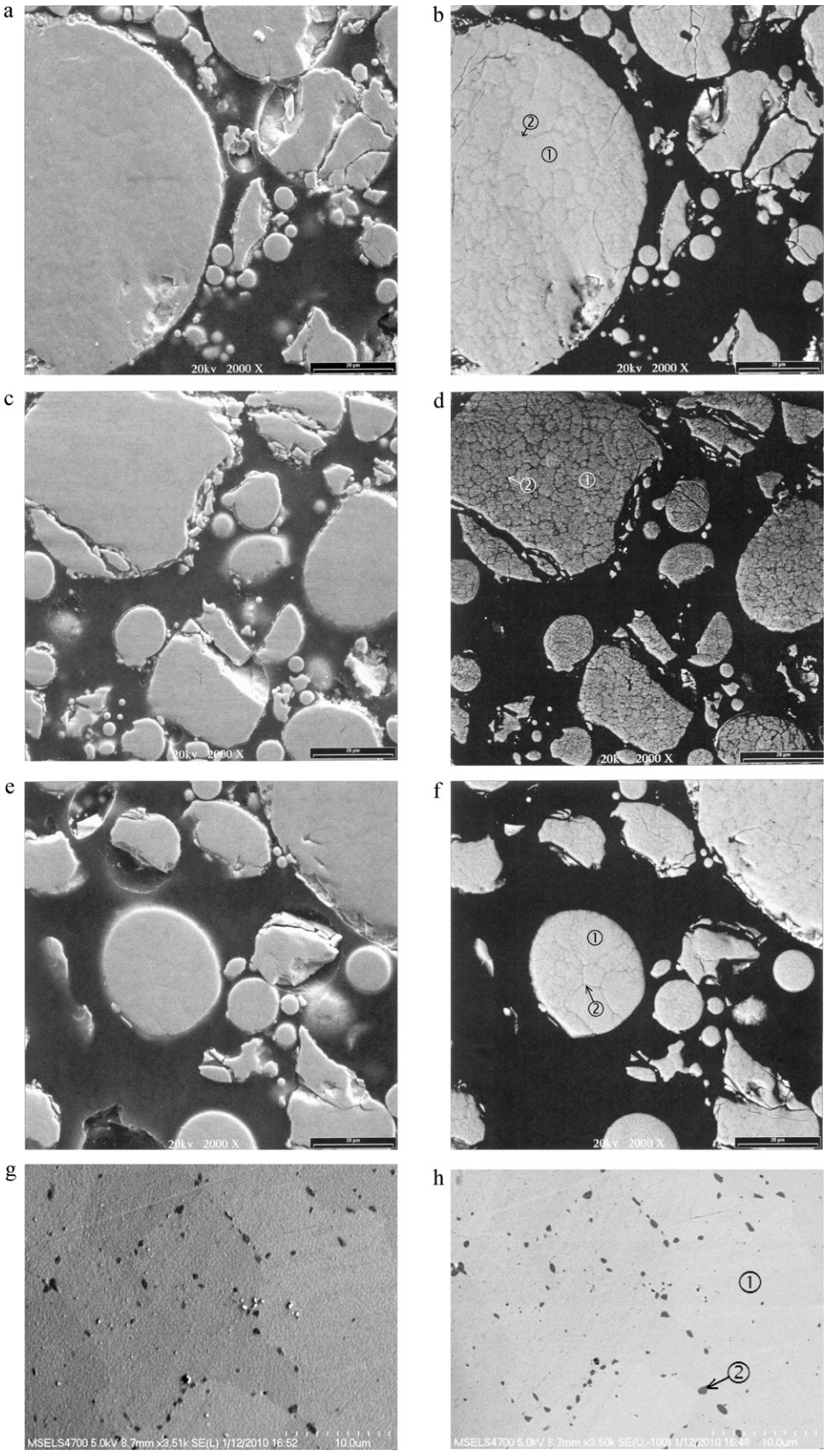

Fig. 4. SEM micrographs for gas atomized C1 SEI (a) and BEI (b), gas atomized C2 SEI (c) and BEI (d), gas atomized C3 SEI (e) and BEI (f), and gas atomized and annealed in hydrogen C3 SEI (g) and BEI (h).

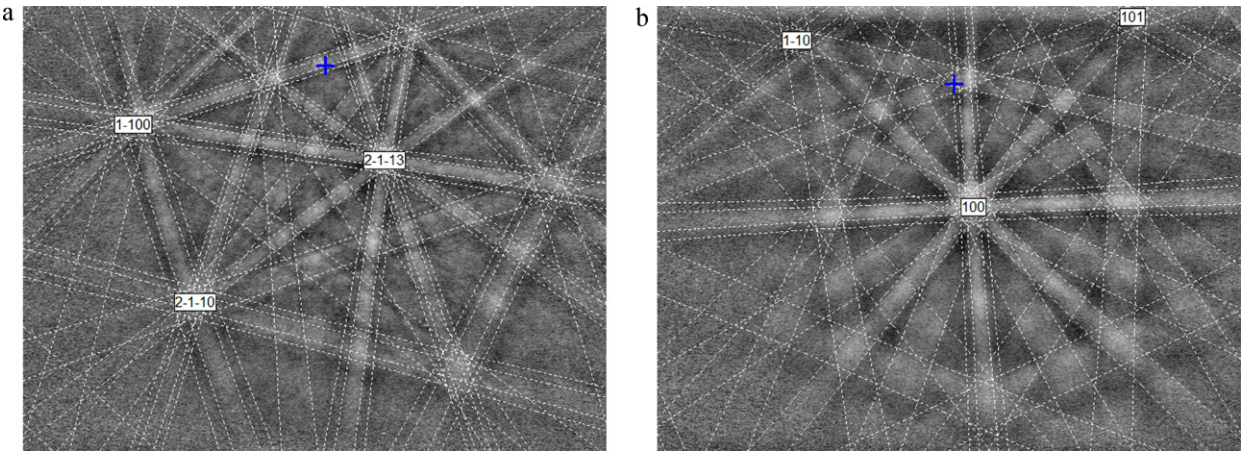

Fig. 5. EBSD patterns from gas atomized C3 annealed in hydrogen: matrix with $LaNi_5$ (a), and precipitate with AlNi (b) simulated patterns overlaid.

the boundary than within the grain. According to the La–Ni binary phase diagram, the liquid with a hyper-stoichiometric composition will form an AB_5 phase with lower B/A ratio than the average and segregate excess of B into grain boundaries [24]. Therefore, the Ni-based phase found in the XRD spectrum is expected to reside in the grain boundary region.

Fig. 4(g) and (h) shows the SEI and BEI micrographs of the GAAH-C3 sample, respectively. After the hydrogen annealing process, the granular structure of Fig. 4a–f disappears, and the particle is composed of a matrix (region 1) with precipitation (region 2) within. The chemical composition determined by EDS is listed in Table 3. While the matrix has a perfect AB_5 stoichiometry, the precipitation is very rich in Mn and Al and lean in rare earth elements. During the annealing process, the AB_5 grain grows in size making available the extra B atoms originally residing in the grain boundary to form isolated precipitates.

EBSD patterns obtained from the matrix phase were indexed against $LaNi_5$, and an example of an indexed pattern is shown in Fig. 5(a). This corroborates the AB_5 stoichiometry found by EDS. Since precipitates such as region 2 in Fig. 4(h) were lower in Ni and higher in Al and Mn than the matrix, EBSD patterns obtained from several precipitates were indexed using the BCC B2-ordered phases AlNi and MnNi, and the match was equally good with both; an example is shown in Fig. 5(b). Thus the phase is primarily a solid solution mixture of AlNi and MnNi.

3.4. PCT analysis

The gaseous hydrogen interactions of the as-cast (MC) and vacuum annealed (MCA) ingots studied by PCT analysis are reported. The gas atomization powder was very difficult to activate because the spherical shape resisted pulverization and the creation of new surfaces. The PCT results from GA samples are much less reliable and not included in this report. The absorption and desorption curves for compositions C1, C2, and C3 are plotted in Fig. 6. The slope of the isotherm from the Cu-free C1 alloy before annealing is very large and becomes smaller after annealing in vacuum. The large slope in the as-cast C1 originates from the multi-component nature of the alloy. Some hypo-stoichiometric phases may contribute to higher hydrogen storage capacity. After annealing, as the abundance of main phase increases, the plateau becomes flatter and storage capacity decreases by a small amount. The amount of absorption/desorption hysteresis is reduced substantially by the annealing process, which is in agreement with the increase in c/a aspect ratio.

In the Cu-containing C2 and C3 alloys, the isotherms from the as-cast samples indicate lower maximum storage capacities than those of the Cu-free C1 alloy. The slopes in the as-cast C2 and C3 are much smaller than that in C1, which exhibit better uniformity in microstructures. After annealing, the changes in the slope in C2 and C3 are much smaller than that in C1 and the hydrogen storage capacities increase. The final capacities after annealing are similar for the C1, C2, and C3 compositions. The slope of the isotherm becomes smaller for C2 and remains about the same for C3 after annealing. Different from Cu-free C1, the hysteresis of the isotherms does not reduce with the annealing process for both Cu-containing C2 and C3. This finding is in agreement with the unchanged c/a aspect ratio from XRD analysis.

The relationship between hysteresis and c/a aspect ratio has been established previously on both AB_5 [5] and AB_2 [28–30] alloys. The conclusion here is that while annealing of the Cu-free alloy made by melt-and-cast can improve the cycle life by reducing the pulverization, the same annealing process applied to the Cu-containing alloy cannot benefit the cycle life. Therefore, in order to extend the cycle life of these Cu-containing alloys, it will be necessary to pursue other powder manufacture processing methods, such as the gas atomization process presented here.

3.5. Magnetic susceptibility measurement

The surface structures of the GAAH samples were further studied by the use of MS measurements, which can determine the amount of the metallic nickel on the surface by normalizing the M_S value to the bulk magnetic susceptibility of pure nickel (58.6 emu/g) [31]. These metallic nickel particles are a by-product of the surface oxidation of other elements, and are a good quantifier to estimate the amount of surface oxide [32]. The shape of the susceptibility curve can be used to estimate the size of the magnetic domain [33]. The magnetic susceptibility curves measured at room temperature for gas atomized C1 power before and after hydrogen annealing are shown in Fig. 7(a) and (b), respectively. The M_S value of 350 memu/g is obtained from GA-C1 without annealing, which slightly less than the value obtained from the 4 h 100 °C 30% KOH etched MC ingot with the same composition (434 memu/g). This M_S value is much higher than values observed from AB_2 alloys (14–20 memu/g) [20] and is the partial reason for the higher surface catalysis activity in AB_5 alloys [31]. The M_S value reduces to 90 memu/g after hydrogen annealing, which indicates that 75% of the metallic Ni re-alloys with the reduced rare earth elements. The re-alloying in the AB_5 alloy with the AH process is not as complete as those in AB_2 with M_S values lower than 0.6 memu/g [20]. The sizes of the metallic

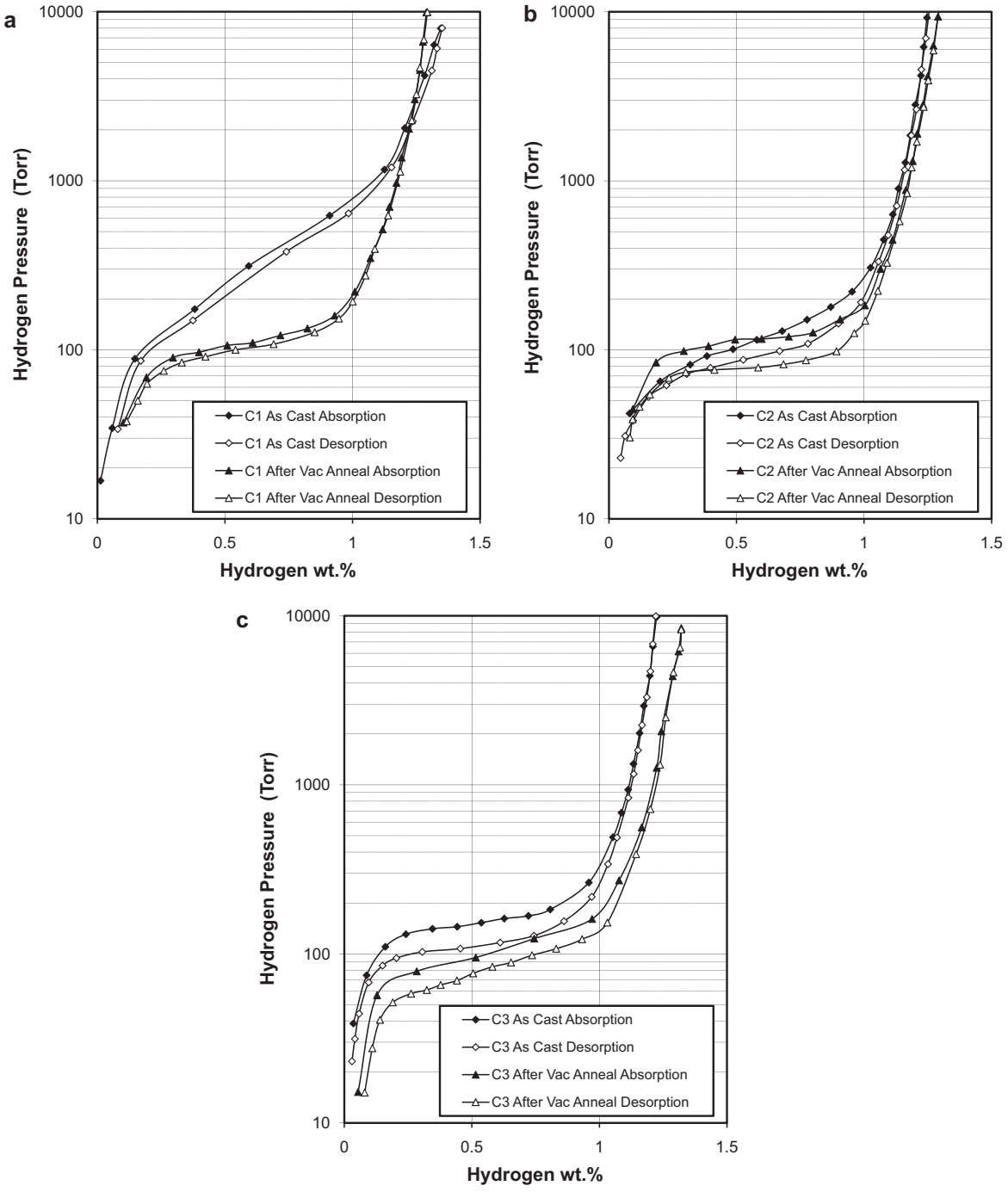

Fig. 6. PCT isotherms measured at 30 °C for alloys with compositions C1 (a), C2 (b), and C3 (c) prepared by two different methods.

nickel on the surface are estimated to be 87 Å and 324 Å for GA-C1 powder before and after the AH process. The Ni cluster size before annealing is slightly smaller than the 4 h 100 °C 30% KOH etched MC ingot with the same composition (114 Å) [31]. The evolution in the amount and size of the surface Ni inclusions of C2 and C3 compositions with annealing is similar.

3.6. Half-cell test

In the flooded half-cell measurement, the AB_5 electrodes were not activated by the hot alkaline bath as in the AB_2 electrodes [20]. The electrodes were first discharged against a partially precharged $Ni(OH)_2$ as the counter electrode with a small current (*C*/70 rate). The observed initial capacity is the result of hydrogen absorption generated from the metal oxidation during the test cell assembly and is listed in Table 4. The amount of initial discharge has been correlated to the ease of surface metal oxidation [34,35]. In the case of this study, the unactivated MCA AB_5 samples show smaller initial discharge capacities compared to those of the activated AB_2. Both GA and GAAH AB_5 samples show very small initial discharge capacities due to the spherical shape of the powder particles contributing to the pulverization difficulty; this is similar to the La-rich AB_5 alloy [20].

The full capacity of the electrode was measured at *C*/70 rate at the first cycle and the results are listed in Table 4. The GA process reduces the full capacity due to oxygen contamination of the

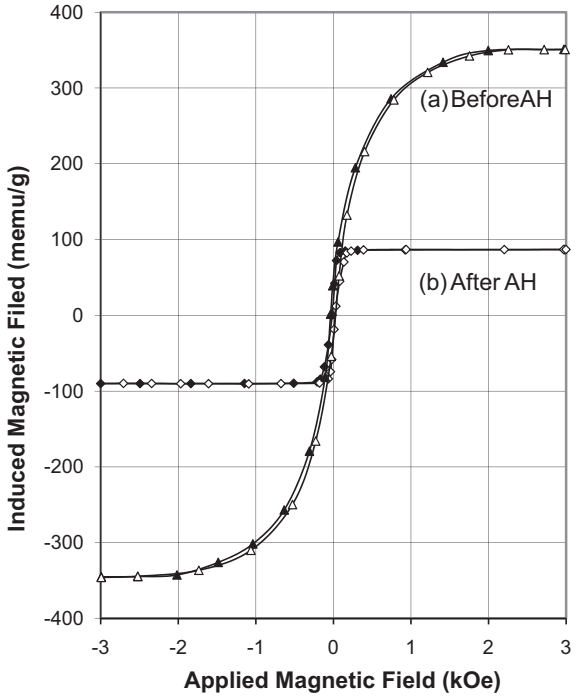

Fig. 7. The magnetic susceptibility curves measured at room temperature for gas atomized C1 power before (a) and after annealing in hydrogen (b). Data in solid and open symbols were taken during increasing and decreasing magnetic field, respectively.

bulk alloy, and the AH process recovers the full capacity, similar to the results of AB_2 GA alloy samples [20]. Except for C2, the full capacities of the GAAH samples are almost the same as their original MCA samples. The lower capacity in GAAH-C2 is due to the slow activation indicating more cycles are needed to improve the capacity.

The half-cell high-rate dischargeability (HRD), defined as the ratio between discharge capacities at a higher rate (*C*/7) and a lower rate (*C*/70), at cycle 10 for each alloy is listed in Table 4. In the half-cell measurement, there is no binder used in the preparation of electrode. Therefore, a discharge rate higher than *C*/7 will cause the disintegration and failure of the electrode. All samples show higher HRD values than the AB_2 alloys (Table 3 in Ref. [16]). No difference in HRD is observed for C1 and C3 alloys made by various preparation methods. In the case of C2 composition, GA sample shows the lowest HRD value due to the formation of surface oxide during cooling. The AH process afterward is able to bring the HRD close to that in the MCA sample.

3.7. Full Ni/MH battery

All nine powders crafted with three different processes and three compositions were made into sealed C-size cylindrical cells by the fabrication method described previously [19]. Performance results from various tests are listed in Table 4. The room temperature high-rate performance was studied by comparing the capacity at 2*C* rate discharge normalized to the capacity at 0.2*C* rate discharge. These cells are not designed for high-rate application but rather provide a test bed for different alloys, so the results should not be cited as the current status of Ni/MH battery. The three MCA samples show similar 2*C* rate capabilities. The GA samples show an improvement in 2*C* discharge, which is different from the case with the AB_2 alloy [20]. The improvement is believed to result from the smaller average particle size of the GA powder. The GAAH samples show even higher 2*C* rate dischargeability. The low-temperature performance is similar (independent of the composition) to the high-rate performance. The Cu-containing C2 and C3 show better −10 °C performance, which proves the concept of using Cu to improve the low-temperature characteristics of the alloy. Both the GA and AH processes can improve the high-rate and low-temperature dischargeability of the AB_5 alloy.

Peak power, or specific power, as a function of state of charge (SOC) was measured using a pulse discharge method [21]. The peak power decreases when more energy from the battery is depleted [19]. The peak power in W/kg under 80% SOC condition at the 5^{th} cycle for each alloy is listed in Table 4. Similar to the 2*C* rate results, both the GA and AH processes improve the peak power at room temperature and at 0 °C. At 0 °C, the peak powers of the GAAH Cu-containing C2 and C3 are better than GAAH Cu-free C1, which confirms the importance of Cu addition in improving the low-temperature performance of Ni/MH battery.

Charge retention (CR) was quantified by dividing the remaining capacity measure at *C*/5 rate by the original capacity before the seven day storage at room temperature and is listed in Table 4. Comparing the CR data from MCA samples, Cu seems to improve the charge retention capability. Both the GA and AH processes improve the CR properties and the difference between Cu-free and Cu-containing alloys is much reduced with a combined GAAH process.

Room temperature cycle life was studied by a *C*/2 charge and *C*/2 discharge scheme. The end of cycle was determined when 60% of the original capacity was reached and is listed in Table 4. While MCA-C1 sample reaches the designed cycle life (450), the addition of Cu in C2 and C3 increases the pulverization rate during cycling and causes a premature failure of MCA-C2 (210) and MCA-C3 (200). The GA powder extends the cycle life by its spherical shape but also introduces an oxide layer on the surface. Extra electrolyte is consumed during the dissolution/activation of the surface oxide and causes degradation in cycle life. Therefore, while

Table 4
Preparation methods, half cell, and full cell measurement results. The first three specific capacity data are in mAh/g and peak powers are in W/kg. The high-rate dischargeability (HRD) is defined by the ratio between the capacities measured at *C*/7 and *C*/70 rates.

Composition #	Preparation	First disch.	Cap. at *C*/7	Cap. at *C*/70	HRD	2*C* (30 °C)	0.5*C* (−10 °C)	Peak power at 80%RT	Peak power at 80%0 °C	Charge retention at 7 days	Cycle life
C1	MCA	13	315	317	99%	59%	90%	161	134	71%	450
C1	GA	2	302	306	99%	89%	91%	185	151	86%	250
C1	GAAH	4	313	317	99%	92%	92%	214	170	91%	280
C2	MCA	14	322	324	99%	56%	91%	158	135	74%	210
C2	GA	2	224	238	94%	75%	94%	178	151	86%	210
C2	GAAH	0	256	260	98%	82%	96%	235	193	89%	320
C3	MCA	19	309	312	99%	56%	91%	163	142	85%	200
C3	GA	9	302	305	99%	76%	92%	165	151	86%	250
C3	GAAH	3	311	312	100%	84%	94%	190	205	89%	300

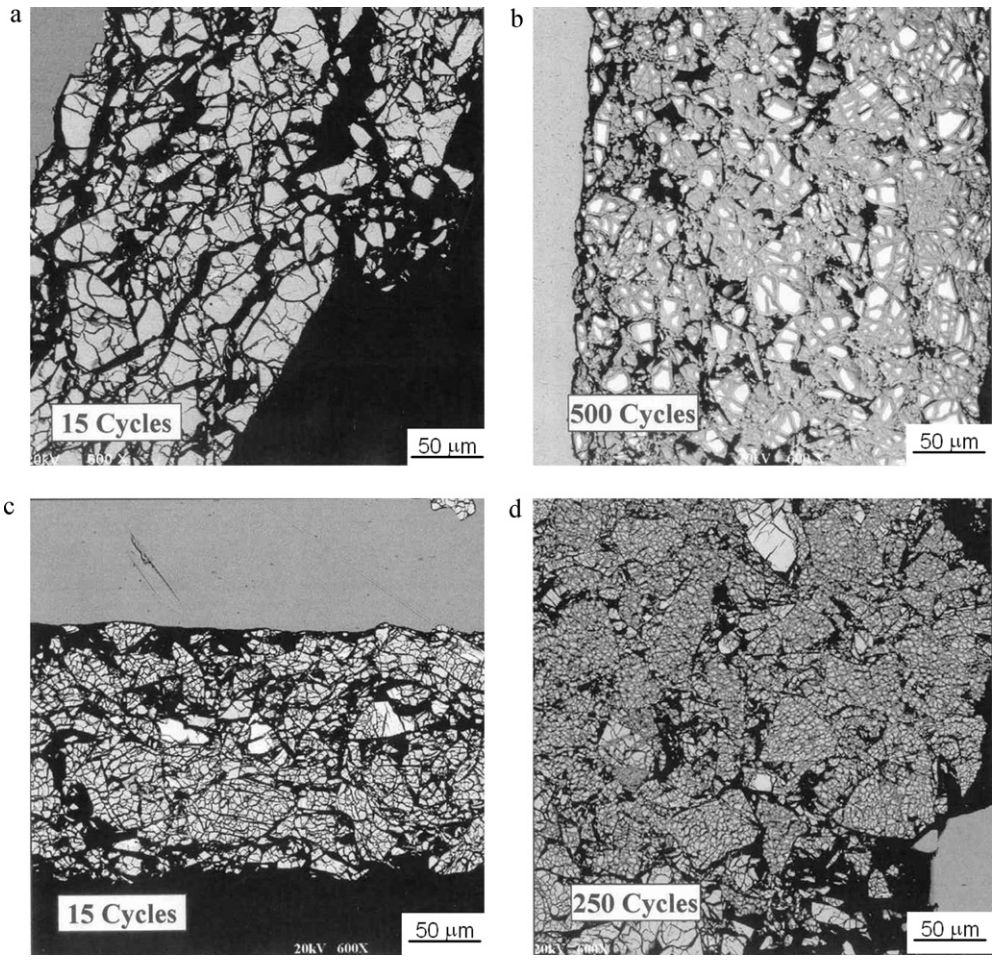

Fig. 8. Cross-section SEM-BEI micrographs of conventional melt-and-cast prepared C1electrode after 15 cycles (a) and 500 cycles (b), and C2 electrode after 15 cycles (c) and 250 cycles (d).

GA-C1 sample shows inferior cycle life performance (250), GA-C2 and GA-C3 show similar or even better results (210 and 250) comparing to MCA. For all GA samples, the cycle life performances are similar and the mechanisms are the same: formation of oxide and short of electrolyte. The AH process reduces the surface oxide formed during GA and thus improves the cycle life for all three compositions.

In order to confirm the failure mode of the Ni/MH battery, SEM BEIs of the cross-sections of the MCA prepared C1 and C2 electrodes with light and heavy cyclings are presented in Fig. 8a–d. For the light cycling (15 cycles), the MCA-prepared C1 alloy shows clean and oxide-free surface with some pulverization from activation (Fig. 8(a)). After 500 cycles, the particle size remains unchanged and the surface is covered with a thick oxide layer. Although about 50% of the material remains metallic (brighter contrast under backscattering condition), the surface oxide impedes the transport of hydrogen. Therefore, the degradation in capacity is due to the growth of the surface oxide. In the case of the Cu-containing C2 alloy, pulverization is already very severe after only 15 cycles, which was predicted from the relatively small c/a aspect ratio. At the end of cycle life (250 cycles), all materials are fully oxidized. Therefore, the initial pulverization is considered to be the main reason contributing to the short life of the Cu-containing alloy prepared by the conventional melt-and-cast.

In the case of GA and GAAH prepared AB_5 samples, we found that the SEM micrographs were identical to those obtained from GA and GAAH prepared AB_2 samples (Fig. 6 in Ref. [16]). The spherical shape of the particle was kept during the cycling process. No noticeable pulverization was found on either GA or GAAH AB_5 samples. In contrast to the MCA samples, the GA and GAAH samples retain large particles with smaller surface area. Therefore, the oxide thickness increases more rapidly in the GA and GAAH samples with cycling, thus resulting in a shorter cycle life compared to the MCA prepared sample.

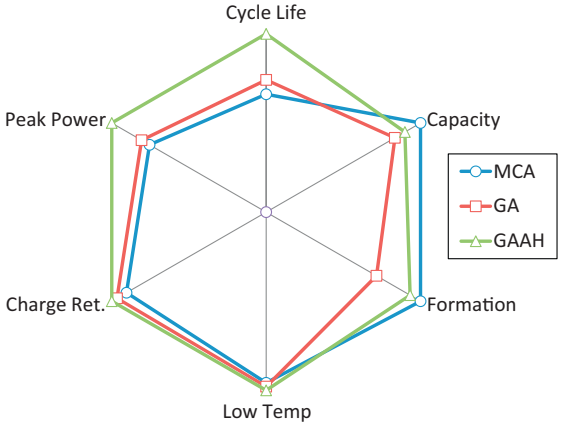

Fig. 9. Radar diagram comparing Cu-containing MH electrode performance among conventional melt-and-cast with vacuum annealing, gas atomization with and without hydrogen annealing. All data are from the average of C2 and C3 alloy compositions. Peak power was measured at 80% SOC at room temperature.

4. Conclusion

Copper was added into (LaCePrNd)(NiCoMnAl)$_5$ formula to improve the low-temperature performance of MH electrode. The cycle life was shortened as a result of a higher degree of pulverization due to stress built into the alloy during hydride/dehydride cycles from a larger PCT hysteresis. The gas atomization together with annealing in hydrogen not only extends the cycle life but also improves the high-rate, low-temperature, and charge retention performances of Cu-containing MH electrode. However, the best cycle life obtained from the GAAH processed Cu-containing alloys is still inferior to the Cu-free alloys prepared by the conventional melt-and-cast process. Therefore, other means, such as compositional modification is needed for further improvement in cycle life.

The effect of GA and GAAH on the Cu-containing MH electrode can be presented in a summarized radar diagram illustrated in Fig. 9. All data are from the average of C2 and C3 compositions and normalized to the highest value in the same category. The formation data are from the reciprocal of number of cycles needed to achieve a stable power. The capacity data are from the first cycle. Judging from this graph, we can summarize that except for the formation, both the GA and GAAH processes improve all major performances of Cu-containing alloy in Ni/MH battery.

Acknowledgements

The authors are thankful to Melanie Rainhout for PCT measurement, Aereon Bisel for magnetic measurement, Alan Chan for SEM and EDS measurements, Ryan Blankenship for ICP analysis, David Pawlik for XRD analysis, Su Cronogue for half-cell testing, Ann Lewis for cell fabrication, and Sui-ling Chen and Cheryl Setterington for full-cell testing.

References

[1] D. Linden, in: D. Linden (Ed.), Handbook of Batteries, 2nd ed., McGraw-Hill, Inc., New York, 1995, pp. 28.19, 33.10.
[2] M. Oshitani, in: H. Tamura (Ed.), Hydrogen Storage Alloys—Fundamentals and Frontier Technologies, NTS Inc., Tokyo, 1998, p. 569.
[3] M. Oshitani, in: N. Saito, T. Sakai (Eds.), Development of Large Scale Rechargeable Batteries for Vehicles, General ed., CMC Publishing Co., Tokyo, 2008, p. 43.
[4] M.A. Fetcenko, S.R. Ovshinsky, K. Young, B. Reichman, T. Ouchi, J. Koch, W. Mays, U.S. Patent 6,830,725 (2004).
[5] Y. Osumi, H. Suzuki, A. Kato, K. Oguro, S. Kawai, M. Kaneko, J. Less-Comm. Met. 89 (1983) 287.
[6] S. Wakao, Y. Yonemura, J. Less-Comm. Met. 89 (1983) 481.
[7] T. Sakai, K. Oguro, H. Miyamura, N. Kuriyama, A. Kato, H. Ishikawa, J. Less-Comm. Met. 161 (1990) 193.
[8] H. Nakano, S. Wakao, J. Alloys Compd. 231 (1995) 587.
[9] F. Lichtenberg, U. Köhler, A. Fölzer, N.J.E. Adkins, A. Züttel, J. Alloys Compd. 253–254 (1997) 570.
[10] W. Hu, J. Alloys Compd. 289 (1999) 299.
[11] P.H.L. Notten, R.E.F. Einerhand, J.L.C. Daams, J. Alloys Compd. 210 (1994) 221.
[12] N. Mani, S. Ramaprabhu, J. Alloys Compd. 363 (2004) 275.
[13] X. Zhu, Y. Zhou, F. Chong, X. Li, W. Pan, J. Rare Earths 22 (2004) 245.
[14] P. Li, X. Wang, Y. Zhang, J. Wu, R. Li, X. Qu, J. Alloys Compd. 354 (2003) 310.
[15] K. Young, T. Ouchi, M.A. Fetcenko, U.S. Patent 7,344,677 B2 (2008).
[16] M.A. Fetcenko, K. Young, S.R. Ovshinsky, T. Ouchi, U.S. Patent 7,393,500 B2 (2008).
[17] W. Hu, D. Kim, K. Jang, J. Lee, J. Alloys Compd. 269 (1998) 254.
[18] F. Lichtenberg, U. Köhler, K. Kleinsorgen, A. Fölzer, A. Bouvier, US Patent 5,738,953 (1998).
[19] K. Young, J. Koch, T. Ouchi, A. Banik, M.A. Fetcenko, J. Alloys Compd. 496 (2010) 669.
[20] K. Young, T. Ouchi, A. Banik, J. Koch, M.A. Fetcenko, Int. J. Hydrogen Energy, doi:10.1016/j.ijhydene.2010.12.051, in press.
[21] K. Young, M.A. Fetcenko, J. Koch, K. Morii, T. Shimizu, J. Alloys Compd. 486 (2009) 559.
[22] J. Kleperis, G. Wójcik, A. Czerwinski, J. Skowronski, M. Kopczyk, M. Beltowska-Brzezinska, J. Solid State Electrochem. 5 (2001) 229.
[23] J.K. Chang, D.S. Shong, W.T. Tsai, J. Power Sources 103 (2002) 280.
[24] H.P. Klug, L.E. Alexander, X-ray Diffraction Procedures for Polycrystalline and Amorphous Materials, 2nd ed., John Wiley & Sons, New York, 1974, p. 656.
[25] Y. Zhou, Y. Lei, Y. Luo, S. Cheng, Q. Wang, Y. Zhang, Acta Metall. Sin. 32 (1996) 857.
[26] Y. Zhou, Y. Zhang, Y. Lei, Q. Wang, Int. J. Hydrogen Energy 23 (1998) 183.
[27] S. Zhang, Z. Ma, H. Guo, L. Wang, B. Yang, C. Lu, S. Zhang, L. Shi, Chin. J. Rare Met. 25 (2001) 199.
[28] K. Young, T. Ouchi, M.A. Fetcenko, J. Alloys Compd. 480 (2009) 428.
[29] K. Young, T. Ouchi, W. Mays, B. Reichman, M.A. Fetcenko, J. Alloys Compd. 480 (2009) 434.
[30] K. Young, T. Ouchi, M.A. Fetcenko, J. Alloys Compd. 480 (2009) 440.
[31] K. Young, M.A. Fetcenko, B. Huang, R.K. Regmi, G. Lawes, Y. Liu, J. Alloys Compd. 506 (2010) 831.
[32] S.R. Ovshisky, M.A. Fetcenko, Appl. Phys. A: Mater. Sci. Process. 72 (2001) 239.
[33] F. Stucki, L. Schlapbach, J. Less-Comm. Met. 74 (1980) 143.
[34] K. Young, T. Ouchi, B. Reichman, W. Mays, R. Regmi, G. Lawes, M.A. Fetcenko, A. Wu, J. Alloys Compd. 489 (2010) 202.
[35] K. Young, R. Regmi, G. Lawes, T. Ouchi, B. Reichman, M.A. Fetcenko, A. Wu, J. Alloys Compd. 490 (2010) 282.